JTTEE5 18:578–592
DOI: 10.1007/s11666-009-9386-2
1059-9630/$19.00 © ASM International

Characterization of Microplasma Sprayed Hydroxyapatite Coating

Arjun Dey, Anoop K. Mukhopadhyay, S. Gangadharan, Mithilesh K. Sinha, and Debabrata Basu

(Submitted April 7, 2009; in revised form July 21, 2009)

Microplasma sprayed (MIPS) HAP coatings on SS316L substrates were characterized by x-ray diffraction, Fourier transformed infrared spectroscopy, optical microscopy, scanning electron microscopy (SEM), field emission scanning electron microscopy (FE-SEM), atomic force microscopy and image analysis. The coating showed a high degree of crystallinity ~92%, a high porosity level of 20 vol.% and a moderate bonding strength of about 13 MPa. The displacement controlled three-point bend tests and associated results of optical microscopy indicated that crack deflection, crack branching, and also local crack bridging occurred during crack propagation in the coating. The nano-hardness (*H*) and Young's modulus (*E*) of the MIPS-HAP coatings as measured by nanoindentation technique were about 6 and 92 GPa, respectively. The fracture toughness (K_{ic}) of the coating was ~0.6 MPa·m$^{0.5}$. From the nano-scratch experiments, the critical normal load at which localized microcracking led to delamination was measured to be ~400 mN.

Keywords characterizations, coating, hydroxyapatite, microplasma spraying

1. Introduction

Hydroxyapatite (HAP), a mineral with the ideal composition $Ca_{10}(PO_4)_6(OH)_2$, is found as a major inorganic constituent of mammalian skeletons and teeth. It is a well-established material for coating on metallic orthopedic implant since the biocompatibility and bio-activeness of HAP allow tissue to grow through the pore to anchor the implants made out of Ti-6Al-4V, SS316L, Co-Cr-Mo alloy etc. Various methods are being employed to prepare HAP coatings, which include plasma spraying (PS), high velocity oxy fuel (HVOF), magnetron sputtering (MS), electrophoretic deposition (EPD), sol-gel (SG), pulsed laser deposition (PLD), biomimetic deposition, dip coating etc. Commercially, PS is being widely used to deposit HAP onto implants due to its high deposition rate and economical advantages (Ref 1). Microplasma sprayed (MIPS) HAP coating is one such promising coating for implants in orthopedic applications. For instance, in a prosthetic hip joint a metallic stem is coated with MIPS-HAP coating for better osteo-integration because, compared to macroplasma (MAPS) sprayed HAP coatings, the MIPS process (a) requires much lesser plasmatron power (e.g. 1-4 kW, c.f. 10-40 kW), (b) generally avoids formation of impure and amorphous phases, (c) provides much higher degree of phase purity and crystallinity (e.g. >80%, c.f. ≤70%) and (d) induces higher degree of porosity (e.g. ~20%, c.f. ≤2-10%) that facilitates bony tissue in-growth (Ref 1-6).

A thorough survey of pertinent literature (Ref 1-6) reveals that there has not been any systematic investigation on the development and characterization of MIPS-HAP coating on SS316L substrate. The HAP coating on SS316L by electrophoretic deposition (Ref 7-10), sol-gel technique (Ref 11) and ultrasonic spray deposition (Ref 12) were developed but none of them were characterized for both physico-chemical and mechanical properties. However, recently, the present author and co-workers reported development of MIPS-HAP coatings on SS316L substrate with high crystallinity and porosity (Ref 13, 14) and also some micromechanical properties (Ref 15, 16). In the present study, we report the physicochemical and detailed mechanical as well as micromechanical and tribological characterization of MIPS-HAP coating.

2. Materials and Methods

2.1 Preparation of HAP Coating on SS316L

Sinter-granulated (average granule size of ~67 μm) in-house synthesized HAP powder (Ref 13, 14) was used for microplasma spraying. The substrate used for the coating was commercially available surgical grade 316L stainless steel. The substrates were shaped into 155 × 20 × 2 mm^3 strips, 50 × 7.14 × 2 mm^3 bars and 25 mm diameter by 25.4 mm long cylinders. Prior to coating, the flat parallel ground substrates were blasted with 200-250 μm alumina

Arjun Dey, Bio-Ceramics and Coating Division, Central Glass and Ceramic Research Institute, Kolkata 700 032, India and Mechanical Test Section, Analytical Facility Division, Central Glass and Ceramic Research Institute, Kolkata 700 032, India; **S. Gangadharan, Mithilesh K. Sinha,** and **Debabrata Basu**, Bio-Ceramics and Coating Division, Central Glass and Ceramic Research Institute, Kolkata 700 032, India; and **Anoop K. Mukhopadhyay**, Mechanical Test Section, Analytical Facility Division, Central Glass and Ceramic Research Institute, Kolkata 700 032, India. Contact e-mail: anoopmukherjee@cgcri.res.in.

grits to roughen the surface to an average roughness (R_a) value of ~2.5 μm. This step was followed by ultrasonic cleaning (Microclean-109, Oscar Ultrasonics, Mumbai, India) using sequentially AR-grade acetone, ethanol and deionized water.

HAP coatings on SS316L substrates were prepared by the MIPS technique at a low plasmatron power of ~1.5 kW using a commercial machine (Miller Maxstar 200 SD 2.5 kW, USA). Argon was used as both primary and secondary gases. The flow rate of primary gas and secondary gas were kept fixed at 10 and 20 slpm. The MIPS-HAP coated SS316L samples were post-heat-treated at 600 °C in air medium. Thereafter, it was characterized by different techniques.

2.2 Chemical and Surface Characterization of the HAP Coating

The chemical analysis of the HAP coating was performed by inductively coupled plasma-atomic emission spectroscopy (ICP-AES: Spectro Flame Modula, Spectro-Analytical Instruments, Model: STM 08, Germany). Surface roughness, R_a, of the coating was measured by the conventional profilometry technique (Form Talysurf, Taylor-Hobson, UK). The phase purity and crystallinity of the HAP coating were analyzed following (Ref 17) by x-ray diffraction (XRD; Philips PW 1710, Eindhoven and Almelo, The Netherlands) technique using monochromatic Cu $K_{\alpha 1}$ radiation at 55 mA and 40 kV. The infra-red spectrum of the coating was recorded in the 400-4000 cm^{-1} range in the transmission mode by a Fourier transformed infra-red spectrometer (FTIR; Perkin-Elmer, Model: 1615, USA). Prior to FTIR and ICP-AES, the samples were prepared by scratching an extremely thin layer from the coating surface using a fine-pointed scalpel. To collect the FTIR spectra of the coating, these fragments were then mixed with dried potassium bromide (KBr) powders at a concentration of around 1 wt.%. The microstructural characterizations and coating thickness measurement were carried out by scanning electron microscopy (SEM; s430i, Leo, UK), field emission scanning electron microscopy (FE-SEM; Supra VP35 Carl Zeiss, Germany) and subsequently by an image analyzer (Leica Q500MC, UK). Prior to insertion in the sample chamber for electron microscopy to avoid charging a 50-70 nm carbon or gold coating was deposited on the HAP coating by the arc deposition technique.

2.3 Evaluation of the Mechanical Properties of the Coating

The bonding strength of the coating was evaluated according to ASTM-C633 (Ref 18, 19). Accordingly, MIPS-HAP coatings were put on SS316L cylindrical stubs of diameter ~25 mm (loading stub, L, and the substrate stub, S). The coated stub (S) was joined to another uncoated stub (L) with a commercially available adhesive tape (FM 1000 adhesive film, Cytec Industries Inc., NJ, USA). The tape was made by a mixture of polyamide and epoxy resin with an appropriate curing agent. The stubs were then mounted on a snugly fitted fixture and kept in an oven for about 5 h at 300 °C for curing purpose. Tensile test was carried out at a cross-head speed of 0.1 mm/min using a universal testing machine (Instron 5500 R, USA) under ambient conditions. The bonding strength of the coating was obtained by dividing the critical load at failure by the coated area (Ref 18, 19).

The deformation and crack propagation behavior of the HAP coating was investigated by simple three-point bending tests with the same machine under displacement controlled mode keeping the MIPS-HAP coated surface of the SS316L bars in the same tensile side (Fig. 1). Both unnotched and notched samples were tested keeping the span length between the two rollers at 40 mm. A fine notch of about 3/4th of the thickness of the SS316L substrate was cut at the middle of the substrate. The deep notch was deliberately made so that the crack can initiate quickly from the tip of the notch and then can propagate into the coating. The crack initiation and propagation processes were investigated for both unnotched and notched HAP coated samples using an optical microscope.

To determine the nano-hardness (H), Young's modulus (E) and fracture toughness (K_{ic}) of the polished cross section of the MIPS-HAP coating, indentations were made using a commercial nanoindentation machine (Fischerscope H100-XYp; Fischer, Switzerland) equipped with a Berkovich tip. The data on H and E were evaluated according to DIN 50359-1 standard from the load versus depth of penetration plots using the well-established Oliver and Pharr (O-P) method (Ref 20). The depth and force sensing resolutions of the machine were 1 nm and 0.2 μN, respectively. For the measurements of both nano-hardness and Young's modulus, the load was kept constant at 10 mN. Further, to determine the H and E value of the polished substrate, e.g. SS316L, a higher load (e.g. 100 mN) was applied. At least ten indents were made at five randomly chosen different locations of the sample. Both the loading and the unloading times were kept fixed at 30 s. Before each experiment the machine was calibrated following DIN 50359-1 standard with nano-indentation-based independent evaluation of H (about 4.14 GPa) and E (about 84.6 GPa) values of a reference glass block (BK7, Schott, Germany).

The K_{ic} of the coating was evaluated from the cracks generated from 100 mN indentation using the following equation (Ref 21-23):

$$K_{ic} = \alpha(E/H)^{0.5}\left(P/C^{1.5}\right) \quad \text{(Eq 1)}$$

where P is the applied load and C is the crack length measured from the centre of the Berkovich nanoindent and E and H are the Young's modulus and hardness of the HAP coating, respectively, measured by the nanoindentation technique at the same applied load P at which K_{ic} of the coating is being measured. For Berkovich indenters the α value was taken as 0.016 (Ref 22, 23).

To evaluate the scratch resistance and the cohesive strength of the coating a nano-scratch tester (Tribo-Indenter, Hysitron, USA) was employed with a 60° conical diamond having a 20 μm radius of curvature at the tip.

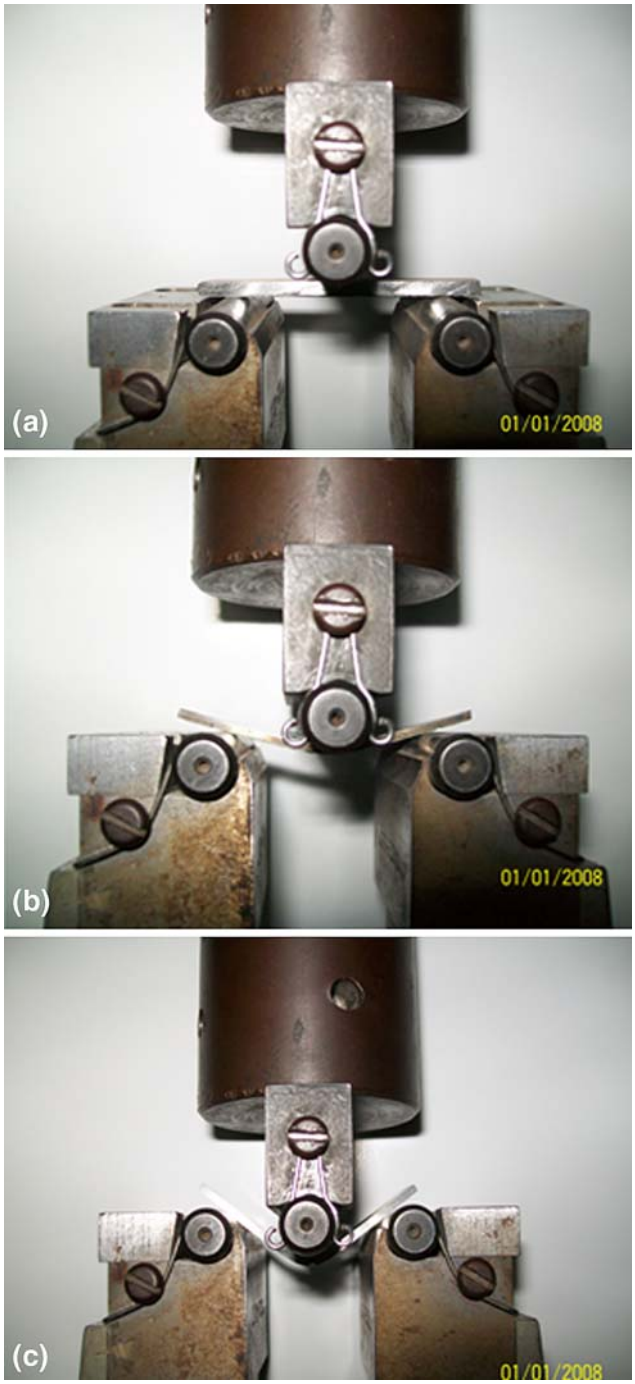

Fig. 1 Arrangement for three-point bending test (a) before, (b) during test and (c) after test for the MIPS-HAP coating

Multiple scratches were made by ramping the normal force from 0 to 700 mN for a scratch length of 100 μm. Normally, during a ramping load test, sudden changes in the load are often observed, which are associated with microcracking and/or delamination of the coatings. The scratch resistance of the coating is measured by the load that indicates delamination and expressed as ''critical load''.

Table 1 Chemical analysis data of MIPS-HAP coating

Constituents	wt.%
CaO	53.14
P_2O_5	40.53
Fe_2O_3	0.06
Pb	Trace
Cd	Trace

3. Results and Discussion

3.1 Chemical and Surface Characterizations

The Ca/P molar ratio of the HAP coating was calculated to be ~1.67 from the ICP-AES result (Table 1), which match exactly with that of the starting HAP powder (Ref 13, 14).

The XRD patterns of HAP coating showed the presence of only HAP peaks (Fig. 2). It can be seen that there is a good match with the standard (JCPDS file no: 09-0432) both in terms of intensity and position of the peaks. The degree of crystallinity of the coating was calculated as ~92% from the XRD data (Table 2) which confirms well with the published results. A high degree of crystallinity is also expected (Ref 6, 13).

The structure of the HAP coating was analyzed using FTIR spectroscopy as shown in Fig. 3. In the FTIR analysis, mainly the peaks for phosphate and hydroxyl groups in the HAP could be identified (Fig. 3) the positions of which are comparable to those reported by other researchers (Ref 13, 24-29). As shown in the FTIR spectra (Fig. 3), the two bands at 632 and 3569 cm^{-1} belong to the vibration of hydroxyl ion. Further, the bands observed at 1046, 1092, and 962 cm^{-1} are the characteristic bands of phosphate stretching vibration, while the bands at 600 and 569 cm^{-1} are due to phosphate bending vibration. The results here indicate that the coatings contain pure HAP phase, although some minor peaks occurred at 3446 and 1423 cm^{-1} possibly for absorption of moisture and at 2923 and 2362 cm^{-1} (Fig. 3) and possibly for absorption of CO_2 as also reported by other workers (Ref 13, 23-25, 28, 29).

The surface roughness, R_a, of the coating was measured as ~7.35 ± 0.74 and ~0.35 ± 0.07 μm (Table 2) for the as-deposited and polished coatings, respectively.

3.2 Coating Microstructure

The SEM photomicrographs of as-deposited HAP coatings as shown in Fig. 4(a)-(h) show that the coating was mainly composed of accumulated splats of elliptical and spheroidal shapes (Fig. 4a). Typical intra-splat and inter-splat macropores are shown in Fig. 4(b) and (c), respectively, while torn-out small parts of splats with different magnifications are also shown in Fig. 4(c) and (d). The presence of inclined cracks in between splats is shown at a lower magnification in Fig. 4(c) and at a higher magnification in Fig. 4(d). These torn-out small parts generated due to impact between HAP granules and the substrate during deposition process would go to the substrate and subsequently might get embedded at the

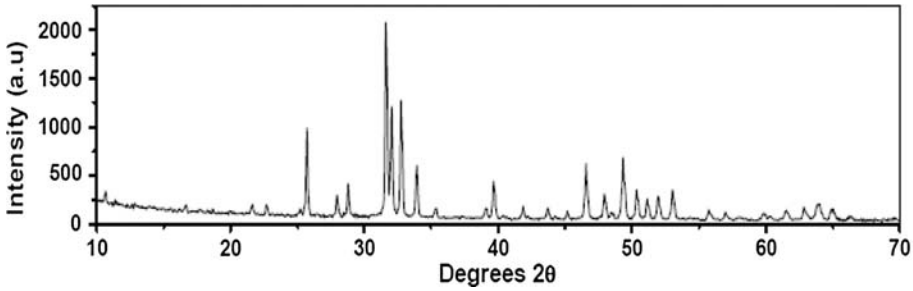

Fig. 2 XRD pattern of MIPS-HAP coating

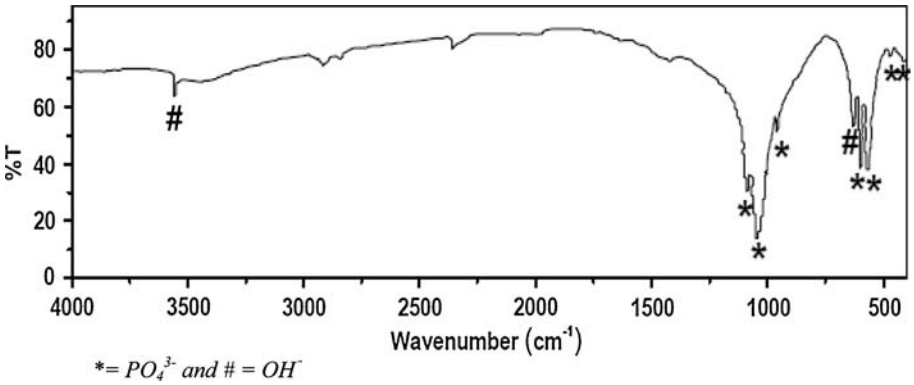

Fig. 3 FTIR pattern of MIPS-HAP coating

Table 2 Surface and microstructural properties of MIPS-HAP coating

Surface roughness, R_a, μm	Coating thickness, μm	Crystallinity, %	Porosity, %	Splat size, μm	Aspect ratio of splats, μm	Macropore size, μm	Micropore size, μm
7.35 ± 0.74 (as-deposited) 0.35 ± 0.07 (polished)	232 ± 8.25	91.6	19.17 ± 1.98	64.28 ± 8.12	1.27 ± 0.15	10-50	~1

coating surfaces, which are evident in these figures. The cracks inside a given splat, i.e. typical intra-splat cracks, are shown in Fig. 4(e) and (f). The portion of intra-splat cracks marked in Fig. 4(e) is shown at higher magnification in Fig. 4(f). It clearly shows also that the cracks grew both parallel and perpendicular to the spraying directions. Occasionally, the cracks were also oriented at a certain angle to the spraying direction. Further, the cracks got deflected in a random fashion in a microstructure. This was probably governed by the local thermo mechanical history during the spraying process. Similarly, there were cracks formed in between the splats as shown in Fig. 4(g). The widths of inter-splat cracks as shown in Fig. 4(g) are larger than those of intra-splat cracks (Fig. 4e, f). These cracks occurred possibly due to the thermal expansion mismatch between the substrate metal and the deposited ceramics.

Unmelted spherical granule was also observed in the coating microstructure (Fig. 4h) which could also play a significant role to impede further improvement in the crystallinity of the coating. All these factors as discussed above contribute thus to the formation of a very heterogeneous microstructure in the present MIPS-HAP coating.

The polished top surface of the coating, i.e. plan section, is shown in Fig. 5(a) and (b) at different regions and at various magnifications. The coating showed the characteristic presence of a large number of macrocracks, microcracks, cracks in between two splats as well as cracks confined inside single splats, macro- and micropores etc. Each reported data of microstructural features was based on an average of measurements made from at least ten SEM and/or FE-SEM images. For this, two or more images were taken at each of the five randomly picked up locations of the coating. Thus, we had used at least ten SEM and/or FE-SEM images to get an average data. For this purpose, the photomicrographs were analyzed with an image analyzer (Leica Q500MC, UK).

The macropore size and micropore size of the coating were ~10-50 μm and ~1 μm, respectively (Table 1). The average volume percent open porosity as exhibited in the different SEM and FE-SEM micrographs of the coating was 19.17 ± 1.98 (Table 2). The distribution of splat size

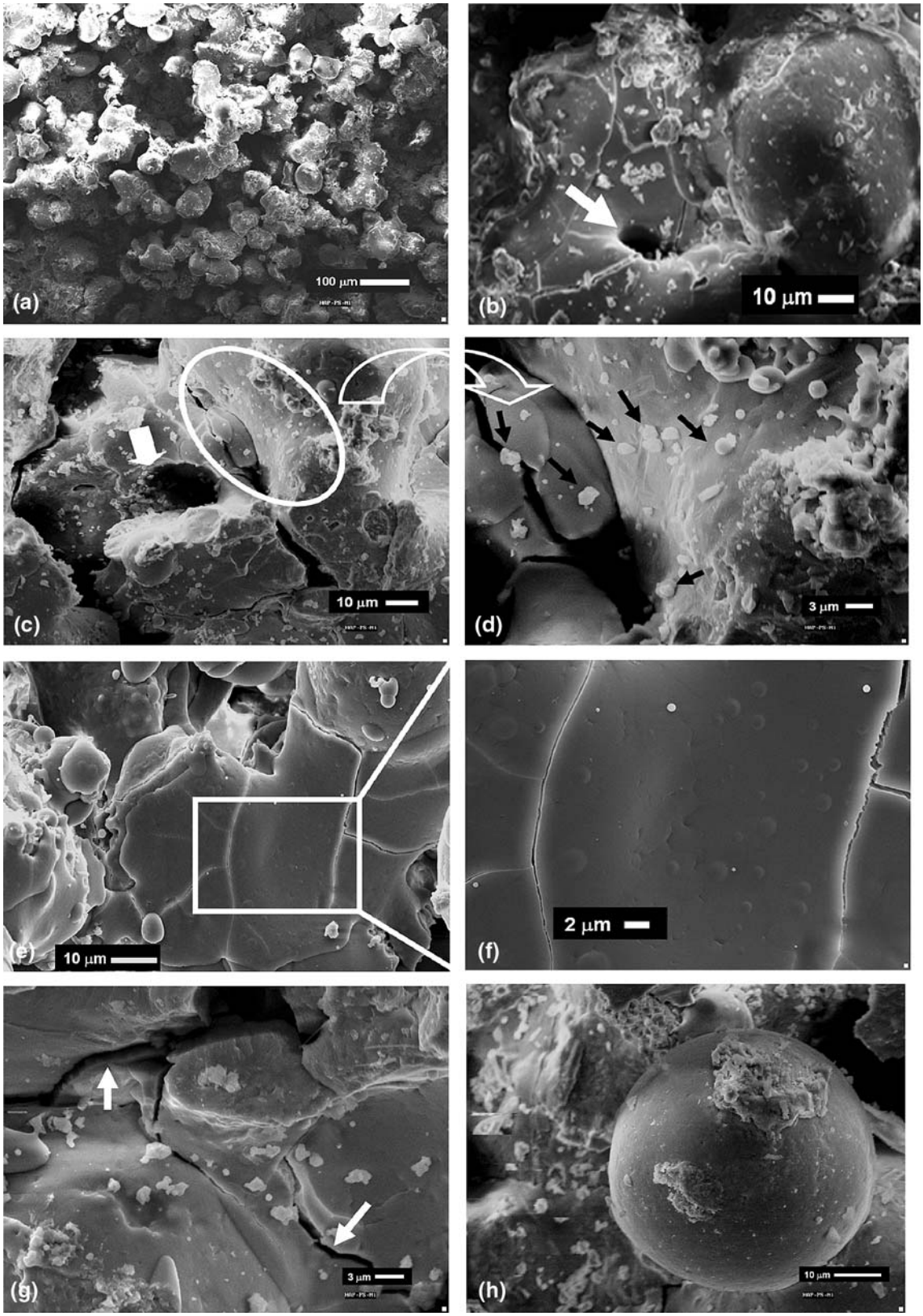

Fig. 4 SEM images of MIPS-HAP coating: (a) as-sprayed microstructure, (b) macropore in a single splat, i.e. intra-splat pore, (c) macropore in-between the splats, i.e. inter-splat pore, (d) tiny worn out parts of splats, (e) cracks in a single splat, i.e. intra-splat cracks, (f) intra-splat cracks at higher magnification, (g) cracks in-between splats, i.e. inter-splat cracks, and (h) an unmelted HAP granule

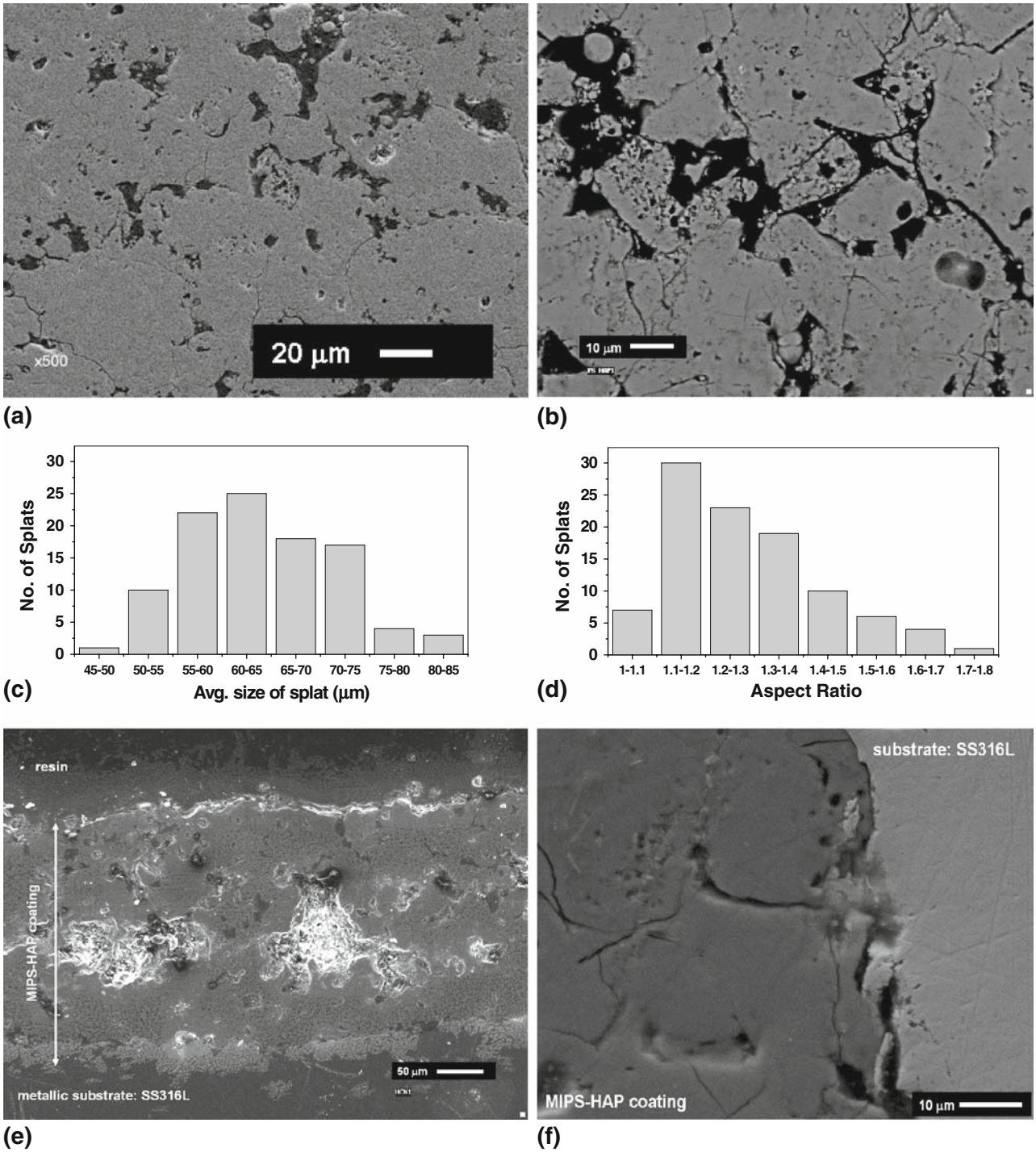

Fig. 5 Polished plan section of the coating (a) at lower magnification and (b) at higher magnification. Histogram of (c) average size (d) aspect ratio of the splats for the as sprayed MIPS-HAP coating. Polished cross section of the coating (e) at lower magnification (f) at higher magnification

and aspect ratio of the splats were as shown in Fig. 5(c) and (d), respectively. The average splat size was 64.28 ± 8.12 μm (Table 2). The typical range of splat size was ~45-85 μm. Similarly, the average aspect ratio of the splats was 1.27 ± 0.15 (Table 2) and the typical range of aspect ratio was 1-1.8. Thus, the shapes of the splats were mostly close to the shape of a small ellipsoid as expected. The slight elongation along the major axis occurs because most of the splats finally assume a pancake shape (Ref 30).

The SEM images of the polished cross-sectional surface of HAP coating are shown in Fig. 5(e) and (f). The coating thickness as measured by the application of the image analysis technique was about 232 ± 8.25 μm (Fig. 5e). These data indicated that the coating thickness was reasonably uniform. The coating-substrate interface (Fig. 5f) was more or less continuous, without any peel off, although the cross-sectional view revealed existence of planar defect, pore and cracks (Fig. 5f) in lower amount.

3.3 Mechanical Properties of the Coating

3.3.1 Bonding Strength. The average value of bonding strength was evaluated as an average of at least ten individual test results. Thus, the average bonding strength of the coating was evaluated as ~12.6 ± 0.31 MPa. After the bonding strength test, a typical loading stub, *L*, and the substrate stub, *S*, are shown in Fig. 6(a). The failure modes of the coating involved both cohesive failure zones (F_{co})

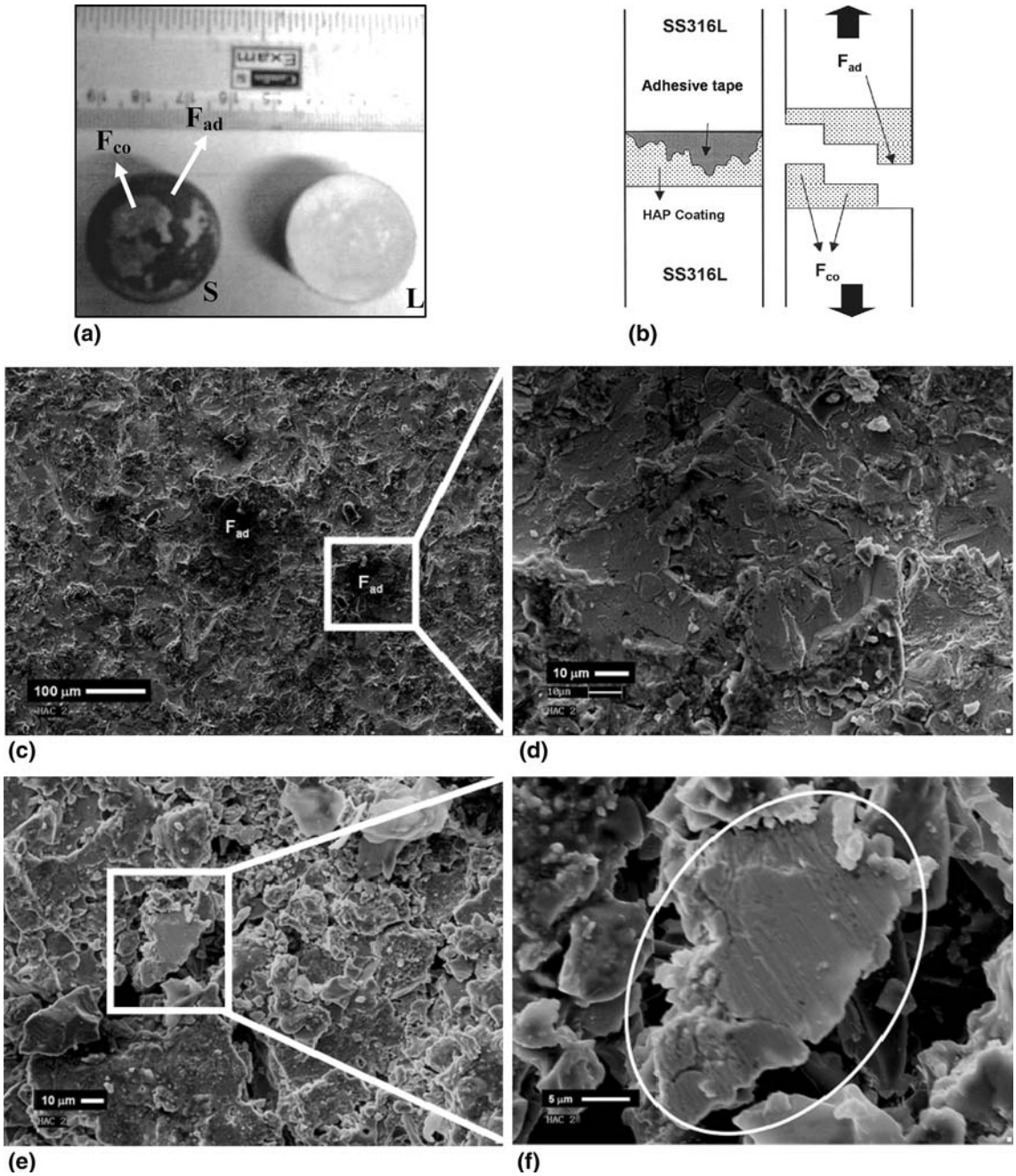

Fig. 6 (a) Fractographs after bonding strength test showing the adhesive fracture (F_{ad}) and cohesive fracture (F_{co}) (*L*: loading stub, *S*: substrate stub), (b) schematic representation of F_{ad} and F_{co}. SEM images of (c) cohesive failure and adhesive failure zones (marked), (d) adhesive failure zone at higher magnification, cohesive failure zone at (e) moderate and (f) higher magnification

where fracture occurred in between the ceramic splats themselves and adhesive failure zones (F_{ad}) where fracture occurred in between the ceramic splats and substrate as indicated schematically in Fig. 6(b). Cohesive failure possibly occurred during the bonding strength test between the layers of splat following the route of inter-splat fracture. Bonding strength was strongly dependent on the mode of fracture. More of adhesive failure was likely to promote good adhesion between the coating and the substrate (Ref 19). The SEM fractograph of a typical cohesive failure zone is shown in Fig. 6(c). However, it also indicated the presence of a couple of adhesive failure zones inside the region of cohesive failure.

The magnified image of the adhesive fracture region (indicated in Fig. 6c) is shown in Fig. 6(d). Here, the roughened surface due to grit blasting prior to MIPS and also deposition of molten ceramic splats onto the surface of the SS316L substrate could be observed. The SEM images of the cohesive failure zone are shown in Fig. 6(e) and (f). On some of the fractured splats angular hatch lines were also observed at a higher magnification (Fig. 6f).

The measured bonding strength of MIPS-HAP coating is ~13 MPa which is within the wide range of values (~2-30 MPa) reported in the literature for the macroplasma deposited coating (Ref 19, 31-34). Generally, bonding strength of the plasma sprayed coating mainly depends on (a) porosity of the coating, (b) thickness of the coating, (c) post-spraying heat-treatment of the coating, (d) choice of the substrate, and (e) residual stress. It has been reported that higher values of bonding strength were typically associated with MAPS-HAP coatings with (a) highly dense microstructure (Ref 36), (b) optimized coating thickness (Ref 35-38), (c) post-heat-treatment in vacuum (Ref 34, 39), etc. On the other hand, comparatively low bonding strengths of MAPS-HAP coating on Ti alloy (e.g. ~7 MPa and ~2-9 MPa) were reported by Filiaggi et al. (Ref 40) and Yang and Chang (Ref 19). Therefore, it is yet to be unequivocally established the control of which factors would totally ensure achievement of high bonding strength in plasma sprayed HAP coatings in general, and in MIPS-HAP coating in particular. However, the moderate value of the bonding strength obtained in the present work was most likely linked to the presence of a much higher porosity (e.g. ~20%) than that (2-5%) obtained in a typical dense MAPS-HAP coating. The bonding strength being a data of paramount importance as far as the practical utilization of such coating in concerned, it needs to be discussed in respect of the data obtained for the present, porous MIPS-HAP coating. The porosity dependence of strength is expressed as (Ref 41):

$$\sigma = \sigma_0 \exp(-bP) \qquad \text{(Eq 2)}$$

where σ and σ_0 are strength of a ceramic at volume percent porosity P and zero, P is the volume percent porosity and b is the pre-exponential factor following (Ref 41). Thus, σ_0 represent the strength of the dense ceramic. The higher end of the range of the reported data on bonding strength of a dense MAPS-HAP coating is about 30 MPa (Ref 34). Thus, if we assume σ_0 was about 30 MPa, the strength of the porous coating would be predicted to be about ~16 MPa, following Eq 2 for a porosity of 20%. Thus, the predicted value of bonding strength matched reasonably well with the experimentally measured data of the present work. However, the experimentally measured data were slightly on the lower side presumably due to presence of the inter-splat cracks.

In MIPS-HAP coating higher porosity level is achieved than what could be achieved by MAPS-HAP coating without sacrificing high degree of crystallinity. The reason for this is that in the development of bone substitutes, a high porosity level is actually required for several practical reasons (Ref 42-44). The pores basically permit tissue in-growth and thus anchor the prosthesis to the surrounding bone, thereby preventing the loosening of implants. Further, the distributed porosity acts like an organization of vascular canals that can ensure the blood and nutrition supply for the bone. In addition, the porosity distribution helps to locally relax the strain and thereby reduce the residual stress. A large surface area to volume ratio in porous HAP coating might enhance the rate of bioresorption (Ref 3, 45). Therefore, the presence of an optimized amount of porosity is an important requisite for bio-application of HAP coating (Ref 13). The additional requirement is that HAP coatings need to be phase-pure and highly crystalline in order to enhance long-term stability in the human body environment.

But there is a very important point that needs to be kept in mind in such developmental works as the present study attempts. It must be clearly borne in perspective though that too high a level of porosity also is not really desirable in a thermally sprayed coating on implant material. The reason is as follows. Although a high porosity might seem favorable for easier osteointegration, a very porous coating is likely to possess extremely poor adhesion to the substrate (Ref 4, 46). If this happens the poor adhesion might delaminate the coating and/or release highly undesirable debris. Such a situation at the end of the day obviously impairs osteointegration by eliciting unfavorable tissue responses. This would be the most undesirable situation and must be avoided. Moreover, an excessive penetration of body fluids through a HAP coating that is highly porous might cause dissolution of the coating material in the interface region. This would deteriorate the adhesion strength further. Therefore, it is generally recommended that a proper compromise between porosity and adhesion strength is achieved (Ref 1, 4, 47). In other words, the present MIPS-HAP coating was deliberately prepared as a porous coating with bonding strength adequate enough for the intended biological application. This target was actually achieved as far as in vivo trial of the present coating was concerned (Ref 48).

Another important factor that affects bond strength is residual stress. Residual stresses of plasma-sprayed coating arise from two main sources. Firstly, there are the intrinsic or deposition stresses which are generated during the cooling of molten, sprayed particles to temperature of the substrate as the solidification process continues to its

final stage. Secondly, differential thermal contraction stresses may arise during post-fabrication cooling down (Ref 49, 50) period. The behavior and mechanism of residual stress generation are so complicated that it is always open to extensive independent study all by itself (Ref 19). However, that was beyond the scope of the present work.

Investigations of plasma-sprayed ceramic coatings on metal substrates have suggested that maximum residual stress generally occurred at the interface of the coating and the substrate (Ref 51, 52). Such a residual stress may initiate a debonding stress at the interface that often leads to adhesive failure of the HAP coating on the metallic substrate. The reported thermal expansion of coefficient (α) sintered HAP ($\alpha_{HAP} = 11.5 \times 10^{-6}\ K^{-1}$ (Ref 19)) was smaller than that of SS316 ($\alpha_{SS316L} = 18 \times 10^{-6}\ K^{-1}$ (Ref 53)). A typical estimate of residual stress (σ_R) would be $\sigma_R = (\Delta\alpha \times \Delta t \times E)/(1 - v)$, where $\Delta\alpha$ is the difference of thermal expansion of coefficient between coating and substrate, Δt is the difference of temperature before and after cooling, E is the Young's modulus of HAP and v is the Poisson's ratio of HAP. Therefore, a high compressive stress (~71 MPa) state may prevail in the present MIPS-HAP coating after cooling down from the elevated temperature attained during PS process. Such a high value of compressive residual stress may cause the MIPS-HAP coating to buckle easily. If a situation as suggested above were prevailing, that would also induce a comparatively lower magnitude of bonding strength as was indeed experimentally observed in the present work.

3.3.2 Crack Initiation and Propagation in the Coating. The typical load versus load-point displacement plots for the unnotched and notched samples are shown in Fig. 7(a) and (b), respectively. Stress developed at the HAP coated SS316L sample was calculated according to the following equation (Ref 54):

$$\sigma = 3PL/2wt^2 \qquad \text{(Eq 3)}$$

where P is the applied load, L is the span length, w is the width and t is the total thickness of the HAP coated sample. It should be noted that the calculation of the stress assumes the coating-substrate composite system as a single material (Ref 54). The calculated values of the stresses are given in Table 3 for the unnotched samples (UN-1.5 and UN-1.8) at pre-fixed cross-head displacements of 1.5 and 1.8 mm and for the notched samples (N-1.5, N-1.75 and N-2) at pre-fixed cross-head displacements of 1.5, 1.75 and 2 mm. Under similar test condition, the stress values of unnotched samples were always higher than those of the notched sample at a similar value of cross-head displacement (Table 3). All the curves in Fig. 7(a) and (b) show an initial linear range, followed by a non-linear portion. This type of behavior has been proposed to be indicative of an elastic-plastic response of the composite system by other researcher (Ref 54). The optical micrographs of crack path for both unnotched and notched samples are shown in Fig. 8(a) and (b) and Fig. 9(a)-(c). The crack deflection and zig-zag path of the crack across the HAP coating were observed in unnotched sample at pre-fixed cross-head displacements of 1.5 and 1.8 mm (Fig. 8a, b), respectively. The crack width at the beginning of UN-1.8 sample was much wider than that of the UN-1.5 sample (Table 3), when a sample already exposed to 1.5 mm cross-head displacement was used. No crack initiation was observed below the cross-head displacement of 1.5 mm. The cracks initiated at still higher loads in the coatings as the tensile stress was further enhanced. The various modes of failure propagation, e.g. crack deflection, crack branching, and also local crack bridging over the coating surface, were observed in notched sample at pre-fixed cross-head displacements of 1.5, 1.75, and 1.8 mm (Fig. 9a-c), respectively. The crack width at the beginning of N-2 sample was much wider than those of the UN-1.75 and UN-1.5 samples (Table 3). These observations may be rationalized in terms of differences between the direction

Table 3 Failure stress and initial crack width data for both unnotched and notched samples

	UN-1.5	UN-1.8	N-1.5	N-1.75	N-2
Stress, MPa	489.25	530.43	261.78	312.50	348.09
Initial crack width, μm	~25	~115	~65	~250	~400

UN = unnotched sample (pre-fixed cross-head displacements at 1.5 and 1.8 mm); *N* = notched sample (pre-fixed cross-head displacements at 1.5, 1.75 and 2 mm)

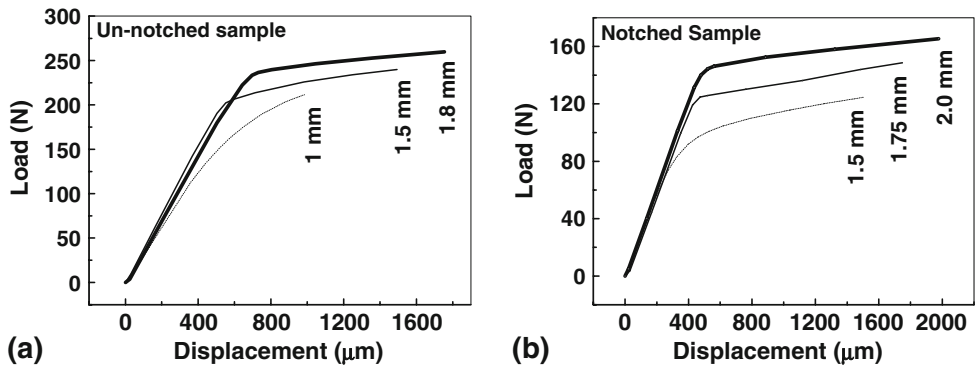

Fig. 7 Load vs. load-point displacement plots for the MIPS-HAP coating on SS316L (a) unnotched and (b) notched substrate samples

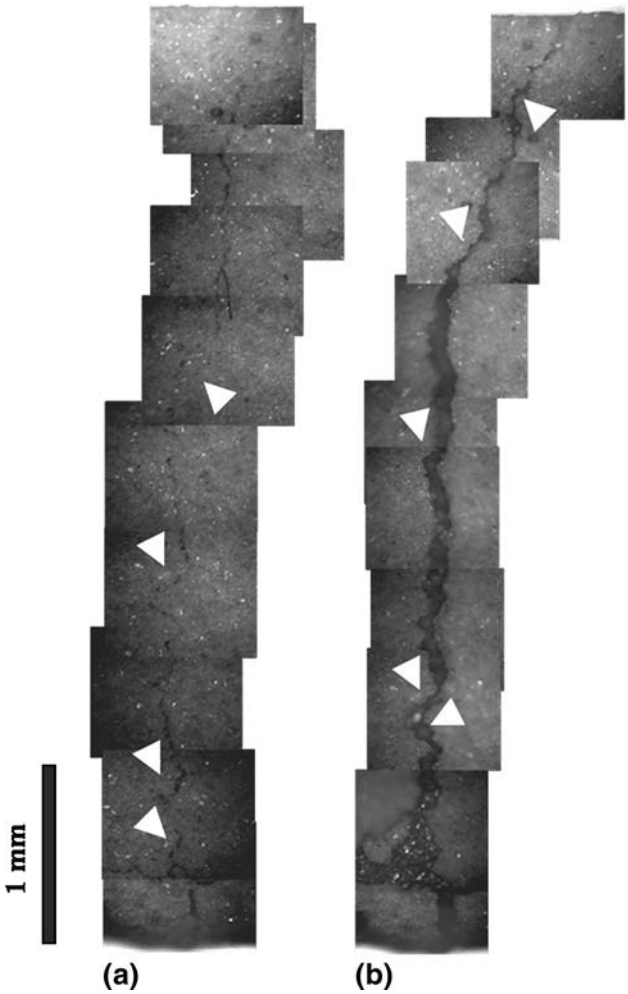

Fig. 8 Optical images of crack propagation for the unnotched samples at pre-fixed cross-head displacements of (a) 1.5 and (b) 1.80 mm

of crack propagation and the local orientation of the splats in the coating microstructure.

3.3.3 Nano-Hardness (*H*) and Young's Modulus (*E*) of the Coating and Substrate. The values of nano-hardness (H) and Young's modulus (E) for the MIPS-HAP coatings were measured as 6.19 ± 1.01 and 92.32 ± 11.36 GPa, respectively (Table 3). A typical topographical 3D atomic force microscopy (AFM) image of an array of Berkovich nanoindents impression on the coating at 10 mN is shown in Fig. 10(a). Further, measurement with Berkovich nanoindentation at 100 mN gave the H and E of the SS316L substrate as 3.51 ± 0.18 GPa and 185.34 ± 5.19 GPa, respectively (Table 4). These data compared favorably with those reported in literature (Ref 15, 16, 55, 56). A typical FE-SEM image of a Berkovich nanoindent impression on SS316L is shown in Fig. 10(b).

Most of the researchers reported nanoindentation data with a Berkovich indenter for HAP coating prepared with a much higher plasma power (e.g. 10-40 kW) machine typically on a Ti6Al4V substrate (Ref 57-60). The reported values on H and E spanned a range of ≈4-5 GPa and 83-123 GPa, respectively, as one moved from the coating-substrate interface to the free coating side across the coating cross section (Ref 59). The nanoindentation data showed further that E value of amorphous zone was much lower than that of the crystalline zone of HAP coating (Ref 57, 58). However, depending on processing condition and type of substrates, the magnetron sputtered thin HAP films (350-650 nm) displayed a much higher range of H (≈4-9 GPa) and E (≈70-150 GPa) values when measured on the plan-section of the coating with a Berkovich indenter (Ref 61, 62). Although a direct comparison of the data of present work with literature data (except Ref 15, 16) was not possible because the processing method and measurement methods were not all identical, it may be still mentioned that the data of the present work compared favorably with literature data (Ref 15, 16, 57-59, 61, 62). However, the data reported (Ref 60) for laser deposited HAP coating were slightly higher than those measured in the present work (Table 4).

3.3.4 Fracture Toughness (K_{ic}) of the Coating. The K_{ic} value of the HAP coating was measured as 0.6 ± 0.02 MPa·m$^{0.5}$ (Table 4) which was much lower than the value typically reported for bulk HAP ~1 MPa·m$^{0.5}$ (Ref 3). This is expected for the MIPS coating because it has a porous microstructure. Porosity dependence of fracture toughness is given by Eq 4 (Ref 63).

$$K_{ic} = (K_{ic})_0 \exp(-bP) \quad \text{(Eq 4)}$$

where K_{ic} and $(K_{ic})_0$ are fracture toughness of a ceramic at volume percent porosity P and zero, P is the volume percent porosity and b is the pre-exponential factor following (Ref 63). The value of fracture toughness reported for bulk dense sintered HAP was ≈1 MPa·m$^{0.5}$ (Ref 3). Therefore, taking $(K_{ic})_0$ as 1 MPa·m$^{0.5}$, $P = 20\%$, the predicted value of toughness would be ~0.65 MPa·m$^{0.5}$ following Eq 4. Thus, the predicted value of toughness was comparable to the experimentally measured data of 0.6 MPa·m$^{0.5}$. It should be mentioned further that the K_{ic} of the present MIPS-HAP coating showed a higher value than the typical reported toughness value of about 0.39-0.55 MPa·m$^{0.5}$ for the macroplasma sprayed or high velocity oxy-fuel sprayed HAP coating (Ref 64-69). Further, the FE-SEM image of a single Berkovich nanoindent impression on the coating is shown in Fig. 10(c). The radial cracks were well defined from near the three corners of the Berkovich indent. However, the cracks in the MIPS-HAP coating were not always cent percent straight. Rather, they were occasionally deflected from the straight path which was also revealed as a dominant mode of crack propagation by the photomicrographs taken during the three-point bending test.

3.3.5 Scratch Resistance of the Coating. The lateral force versus time plots and the normal displacement versus time plots as recorded during the nano-scratch testing under a normal force of 700 mN were shown for the present MIPS-HAP coating in Fig. 11(a) and (b), respectively. A sharp fall at about 250 mN in the lateral force (Fig. 11a) and the corresponding discontinuity in the

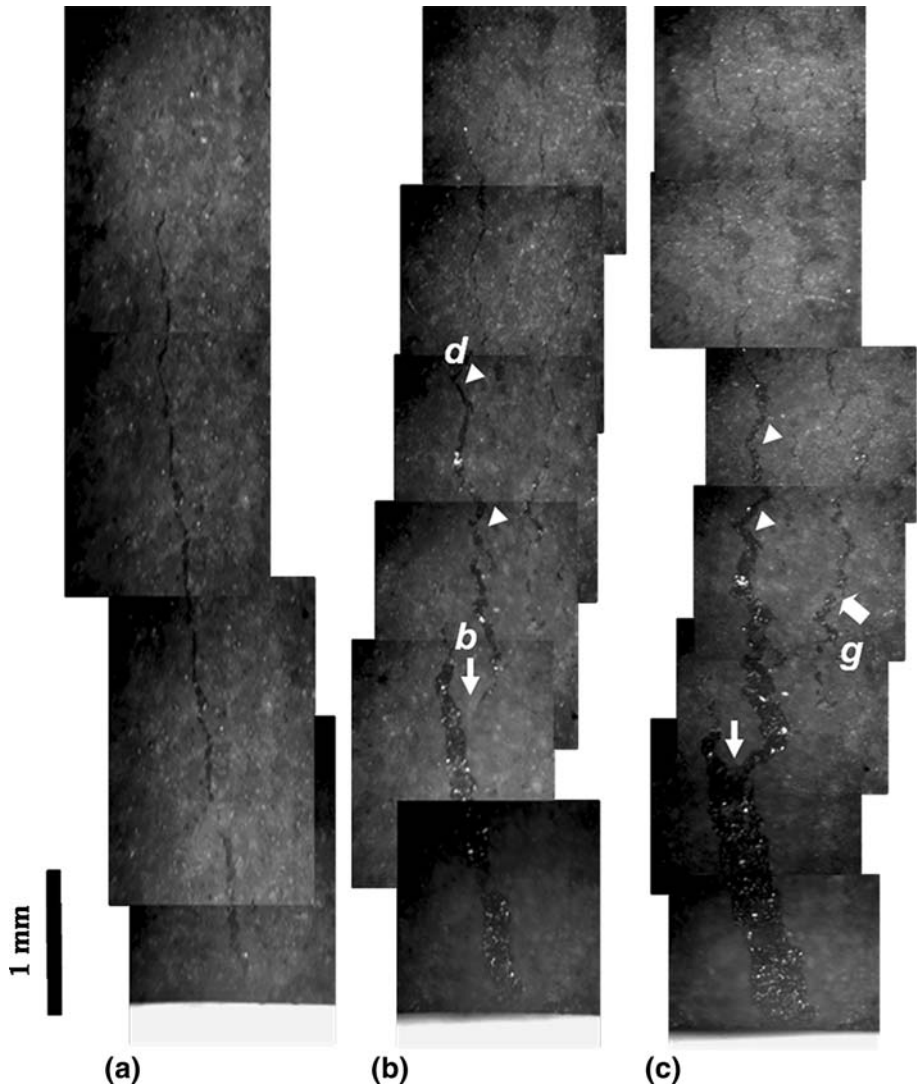

Fig. 9 Optical images of crack propagation for the notched samples at pre-fixed cross-head displacements of (a) 1.5, (b) 1.75, and (c) 2 mm. d = crack deflection, b = crack branching, g = local crack bridging

normal displacement versus time plot (Fig. 11b) indicated that there was a delamination of the coating at this point which occurred at an instant a little over 9 s from the start of the test. The normal displacement was at about 12 μm when the coating was delaminated (Fig. 11b).

The coefficient of friction was measured to be in the range of around 0.45-0.55 (Table 4). The optical micrographs of microstructure of the coating before (starting and end point of the scratch test marked as *x* and *y*, respectively) and after (the arrow indicates the direction of scratching) the nano-scratch testing are shown in Fig. 11(c) and (d), respectively. No severe peel off was noticed in the present coating and the scratch testing generated only microcracks (Fig. 11d). There was not much data available in literature on nano-scratch deformation behavior of HAP-coating for comparison. For a 650 nm thick magnetron sputtered HAP coating on Ti and Si scratches made at normal loads of 40, 60, 80, 100, and 150 mN showed quite different behavior (Ref 61). In the case of HAP coating on Si sample, a complete film separation was observed, suggesting a poor interfacial bonding between HAP and Si. In contrast, for the HAP coating on Ti sample, the end of scratched HAP film was still attached to its substrate. These results indicated a stronger bonding between HAP coating and Ti than that between HAP coating and Si (Ref 61). In the case of biphasic HAP coating, the scratch adhesion strength was reported to be nearly constant around 430-500 mN (Ref 70). In our case, the lateral force to initiate delamination was ~210 mN and the corresponding normal load was ~400 mN. Therefore, the critical load at which microcracks generated in the present MIPS-HAP coating was estimated to be ~400 mN. Thus, the order of magnitude of the ''critical load'' observed in the present experiments was comparable to that reported by other researchers (Ref 70).

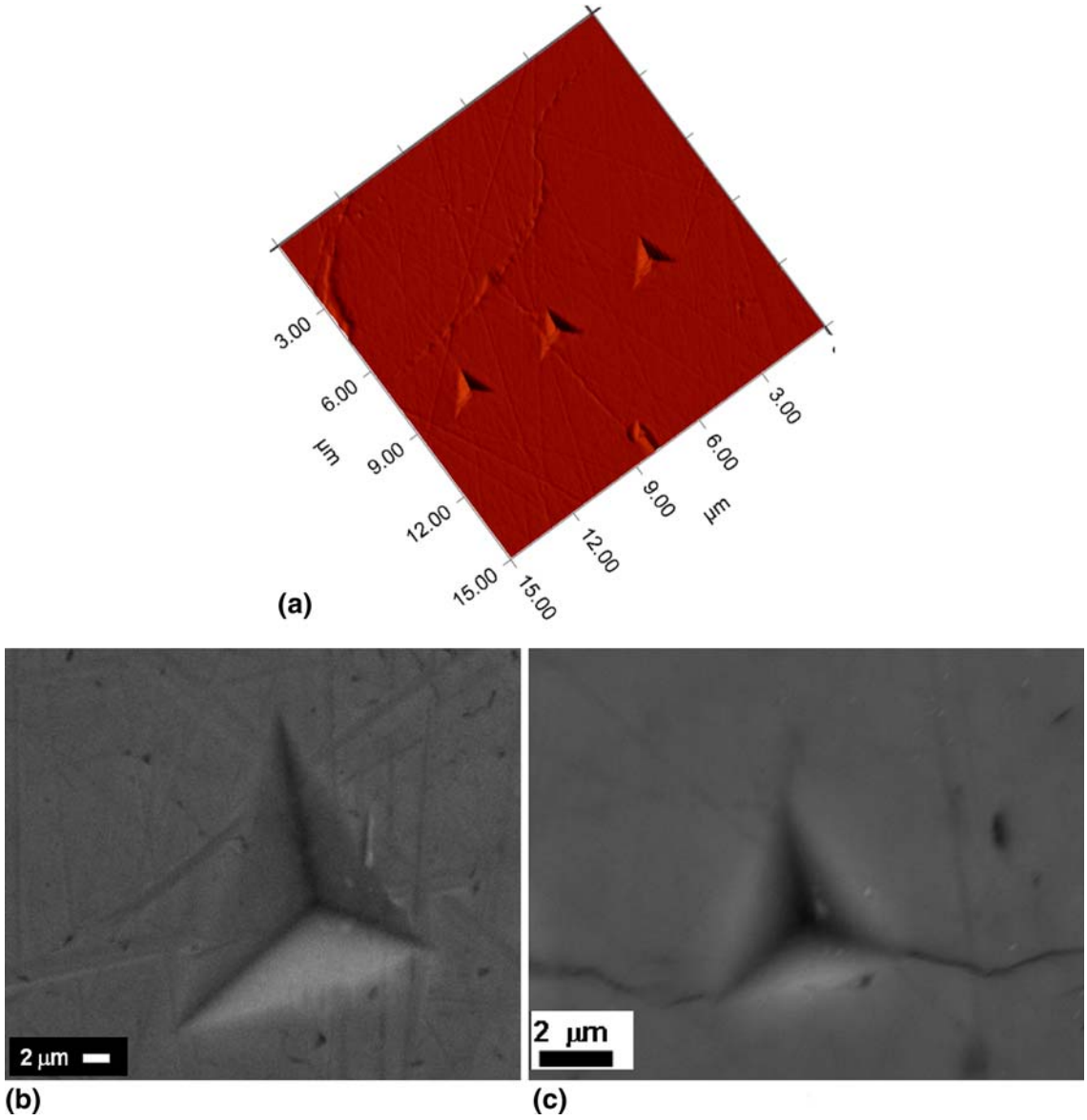

Fig. 10 (a) Topographical 3D AFM image of Berkovich indentation array at 10 mN load on HAP coating; (b) FE-SEM image of an indent impression at 100 mN load on SS316L; (c) FE-SEM image of an indent impression at 100 mN load on HAP coating

Table 4 Mechanical properties of MIPS-HAP coating and the SS316L substrate

	Bonding strength, MPa	Nano-hardness, GPa	Young's modulus, GPa	Fracture toughness, $MPa \cdot m^{0.5}$	Coefficient of friction
MIPS-HAP coating	12.76 ± 1.32	6.19 ± 1.01	92.32 ± 11.36	0.6 ± 0.02	0.45-0.55
SS316L	…	3.51 ± 0.18	185.34 ± 5.19	…	…

4. Conclusions

Microplasma spraying (MIPS) of synthesized sinter-granulated HAP powder (Ca/P ~ 1.67) on SS316L substrate was carried out at a very low plasmatron power of about 1.5 kW. The Ca/P molar ratio of the HAP coating was ~1.67. The XRD patterns of HAP coating showed it to be phase pure and highly crystalline (~92%). The FTIR spectrum of the material also confirmed this observation. The coating showed the characteristic heterogeneous microstructure comprising of ellipsoidal and spheroidal splats with large number of inter/intra-splat microcracks,

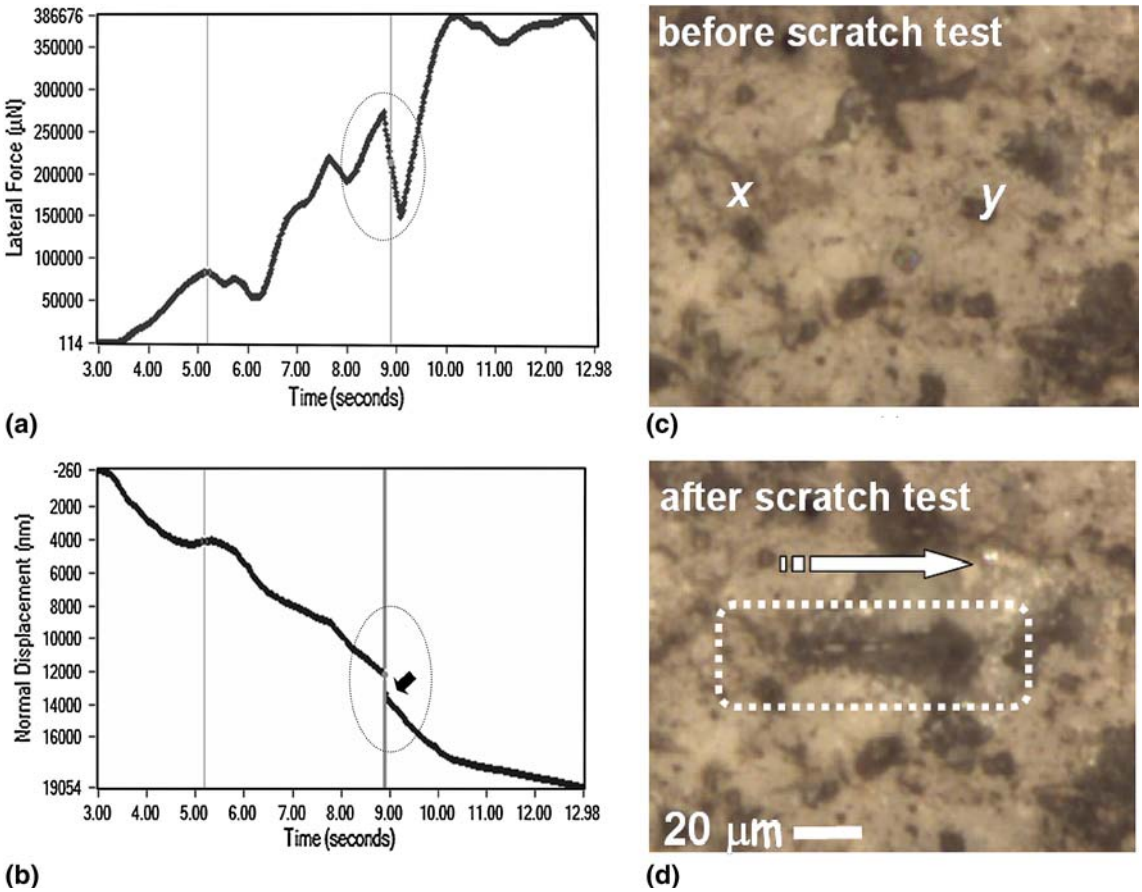

Fig. 11 (a) Lateral force and (b) normal displacement as a function of time during nano-scratch testing of MIPS-HAP coating. Optical micrograph of the coating (c) before the nano-scratch testing (start and end point of the scratch test marked as *x* and *y*, respectively) and (d) after the nano-scratch testing (the arrow indicates the direction of scratching)

macro/micro pores and different types of defects. The typical splat size and aspect ratio were 64.28 ± 8.12 μm and 1.27 ± 0.15 μm, respectively. The volume percent open porosity of the coating was estimated as 19.17 ± 1.98. The coating had average macropore and micropore sizes of ~10-50 μm and ~1 μm, respectively. It exhibited moderate bond strength of ~13 MPa. The displacement controlled three-point bend tests and associated results of optical microscopy indicated that crack deflection, crack branching, and also local crack bridging occurred during crack propagation in the coating. Nanoindentation with a Berkovich indenter at 10 mN gave nano-hardness (H) and Young's modulus (E) for the MIPS-HAP coatings to be 6.19 ± 1.01 and 92.32 ± 11.36 GPa, respectively. The nanoindentation induced crack length measurement resulted in a K_{ic} of 0.6 ± 0.02 MPa·m$^{0.5}$ for the HAP coating. The nano-scratch experiments conducted under a normal load of 700 mN with a diamond conical indenter of 60° included angle having a 20 μm radius of curvature at the tip, giving the coefficient of friction of HAP coating as 0.45-0.55. The critical normal load that caused localized delamination through microcracking was ~400 mN, which gave a quantitative measure of the scratch resistance of the present MIPS-HAP coating.

Acknowledgments

The authors are grateful to Director, Central Glass and Ceramic Research Institute (CGCRI), Kolkata, for his kind permission to publish this paper and to Dr. D. K. Bhattacharya, Head, Analytical Facility Division of CGCRI, for his kind encouragement during the course of this work. One of the authors (A.D.) also sincerely acknowledges the support and encouragements received from Prof. N. R. Bandyopadhyay of the School of Materials Science and Engineering, Bengal Engineering and Science University (BESU), Shibpur. In addition, the authors appreciate the infrastructural support received from all colleagues and particularly those received from the colleagues of the Mechanical Test Section and Bio Ceramics and Coating Division at CGCRI. Finally, the authors gratefully acknowledge financial support received from DST-SERC (Project No: GAP 0216) and CSIR (Network Project TAREMAC No: NWP 0027).

References

1. K.A. Gross and C.C. Berndt, Biomedical Application of Apatites, *Rev. Mineral. Geochem.*, 2002, **48**(1), p 631-672

2. W. Tong, J. Chen, X. Li, Y. Cao, Z. Yang, J. Feng, and X. Zhang, Effect of Particle Size on Molten States of Starting Powder and Degradation of the Relevant Plasma-Sprayed Hydroxyapatite Coating, *Biomaterials*, 1996, **17**(15), p 1507-1513
3. L.L. Hench, Bioceramics, *J. Am. Ceram. Soc.*, 1998, **81**(7), p 1705-1733
4. C.E. Mancini, C.C. Berndt, L. Sun, and A. Kucuk, Porosity Determinations in Thermally Sprayed Hydroxylapatite Coatings, *J. Mater. Sci.*, 2001, **36**(16), p 3891-3896
5. R.S. Lima, K.A. Khor, H. Li, P. Cheang, and B.R. Marple, HVOF Spraying of Nanostructured Hydroxyapatite for Biomedical Applications, *Mater. Sci. Eng. A*, 2005, **396**(1-2), p 181-187
6. L. Zhao, K. Bobzin, F. Ernst, J. Zwick, and E. Lugscheider, Study on the Influence of Plasma Spray Processes and Spray Parameters on the Structure and Crystallinity of Hydroxylapatite Coatings, *Materialwiss. Werkstoff.*, 2006, **37**(6), p 516-520
7. T.M. Sridhar, T.K. Arumugam, S. Rajeswari, and M. Subbaiyan, Electrochemical Behaviour of Hydroxyapatite-Coated Stainless Steel Implants, *J. Mater. Sci. Lett.*, 1997, **16**(23), p 1964-1966
8. S. Kannan, A. Balamurugan, and S. Rajeswari, Development of Calcium Phosphate Coating on Type 316L SS In Vitro Response, *Trend. Biomater. Artif. Org.*, 2002, **16**(1), p 8-11
9. T.M. Sridhar, U.K. Mudali, and M. Subbaiyan, Sintering Atmosphere and Temperature Effects on Hydroxyapatite Coated Type 316L Stainless Steel, *Corros. Sci.*, 2003, **45**(10), p 2337-2359
10. T.M. Sridhar, U.K. Mudali, and M. Subbaiyan, Preparation and Characterisation of Electrophoretically Deposited Hydroxyapatite Coatings on Type 316L Stainless Steel, *Corros. Sci.*, 2003, **45**(2), p 237-252
11. A. Balamurugan, S. Kannan, and S. Rajeswari, Bioactive Sol-Gel Hydroxyapatite Surface for Biomedical Applications—In Vitro Study, *Trend. Biomater. Artif. Org.*, 2002, **16**(1), p 18-20
12. G. Ye and T. Troczynski, Hydroxyapatite Coatings by Pulsed Ultrasonic Spray Pyrolysis, *Ceram. Int.*, 2008, **34**(3), p 511-516
13. A. Dey, A.K. Mukhopadhyay, S. Gangadharan, M.K. Sinha, and D. Basu, Development of Hydroxyapatite Coating by Microplasma Spraying, *Mater. Manuf. Process.*, 2009 (in press)
14. A. Dey, A.K. Mukhopadhyay, S. Gangadharan, M.K. Sinha and D. Basu, Anisotropy of Elastic Modulus on Bioactive HAP Coating, *20th Annual General Meeting*, Feb 10-12, 2009 (Kolkata, India), Materials Research Society of India (MRSI), 2009, p 110
15. A. Dey, A.K. Mukhopadhyay, S. Gangadharan, M.K. Sinha, D. Basu, and N.R. Bandyopadhyay, Nanoindentation Study of Microplasma Sprayed Hydroxyapatite Coating, *Ceram. Int.*, 2009, **35**(6), p 2295-2304
16. A. Dey, A.K. Mukhopadhyay, S. Gangadharan, M.K. Sinha, and D. Basu, Mechanical Properties of Microplasma Sprayed HAP Coating, *Interquadrennial Conference of International Congress on Fracture*, B.K. Raghu Prasad and R. Narasimhan, Ed., Aug 3-7, 2008 (Bangalore, India), I. K. International Publishing House Pvt. Ltd., 2008, p 311-313
17. E. Landi, A. Tampieri, G. Celotti, and S. Sprio, Densification Behaviour and Mechanisms of Synthetic Hydroxyapatites, *J. Eur. Ceram. Soc.*, 2000, **20**(14-15), p 2377-2387
18. ASTM C 633-79. Standard Test Method for Adhesion or Cohesive Strength of Fame-Sprayed Coatings
19. Y.C. Yang and E. Chang, Influence of Residual Stress on Bonding Strength and Fracture of Plasma-Sprayed Hydroxyapatite Coatings on Ti-6Al-4V Substrate, *Biomaterials*, 2001, **22**(13), p 1827-1836
20. W.C. Oliver and G.M. Pharr, An Improved Technique for Determining Hardness and Elastic Modulus Using Load and Displacement Sensing Indentation Experiments, *J. Mater. Res.*, 1992, **7**(6), p 1564-1583
21. A.G. Evans, B.R. Lawn, and D.B. Marshall, Elastic/Plastic Indentation Damage in Ceramics: The Median/Radial Crack System, *J. Am. Ceram. Soc.*, 1980, **63**(9-10), p 574-581
22. D.R. Dukino and M.V. Swain, Comparative Measurement of Fracture Toughness with Berkovich and Vickers Indenters, *J. Am. Ceram. Soc.*, 1992, **75**(12), p 3299-3304
23. J. Chen and S.J. Bull, Assessment of the Toughness of Thin Coatings Using Nanoindentation Under Displacement Control, *Thin Solid Films*, 2006, **494**(1-2), p 1-7
24. L.L. Hench and J. Wilson, *An Introduction to Bioceramics: Advance Series in Ceramics*, Vol 1, World Scientific Publishing Co. Pte. Ltd, Singapore, 1993, p 229-231
25. J.G. Morales, J.T. Burgues, T. Boix, J. Fraile, and R.R. Clemente, Precipitation of Stoichiometric Hydroxyapatite by a Continuous Method, *Cryst. Res. Technol.*, 2001, **36**(1), p 15-26
26. L. Sun, C.C. Berndt, and C.P. Grey, Phase Structural Investigations of Plasma Sprayed Hydroxyapatite Coating, *Mater. Sci. Eng. A*, 2003, **360**(1-2), p 70-84
27. S.J. Ding, T.H. Hung, and C.T. Kao, Immersion Behavior of Plasma Sprayed Modified Hydroxyapatite Coatings After Heat Treatment, *Surf. Coat. Technol.*, 2003, **165**(3), p 248-257
28. M.P. Mahabole, R.C. Aiyer, C.V. Ramakrishna, B. Sreedhar, and R.S. Khairnar, Synthesis, Characterization and Gas Sensing Property of Hydroxyapatite Ceramic, *Bull. Mater. Sci.*, 2005, **28**(6), p 535-545
29. S. Nath, K. Biswas, and B. Basu, Phase Stability and Microstructure Development in Hydroxyapatite-Mullite System, *Scr. Mater.*, 2008, **58**(12), p 1054-1057
30. P. Fauchais, J.F. Coudert, A. Verdelle, M. Verdelle, A. Grimaud, and P. Roumilhac, State of the Art for the Understanding of the Physical Phenomenon Involved in Plasma Spraying at Atmospheric Pressure, *Thermal Spray: Advances in Coatings Technology*, D.L. Houk, Ed., Sept 14-17, 1987 (Orlando, FL), ASM International, 1987, p 11-18
31. C.Y. Yang, R.M. Lin, B.C. Wang, T.M. Lee, E. Chang, Y.S. Hang, and P.Q. Chen, In Vitro and In Vivo Mechanical Evaluations of Plasma-Sprayed Hydroxyapatite Coatings on Titanium Implants: The Effect of Coating Characteristics, *J. Biomed. Mater. Res.*, 1997, **37**(3), p 335-345
32. Y.C. Yang and E. Chang, The Bonding of Plasma-Sprayed Hydroxyapatite Coatings to Titanium: Effect of Processing, Porosity and Residual Stress, *Thin Solid Films*, 2003, **444**(1-2), p 260-275
33. Y.W. Gu, K.A. Khor, and P. Cheang, In Vitro Studies of Plasma-Sprayed Hydroxyapatite/Ti-6Al-4V Composite Coatings in Simulated Body Fluid SBF, *Biomaterials*, 2003, **24**(9), p 1603-1611
34. Y.C. Yang, Influence of Residual Stress on Bonding Strength of the Plasma-Sprayed Hydroxyapatite Coating After the Vacuum Heat Treatment, *Surf. Coat. Technol.*, 2007, **201**(16-17), p 7187-7193
35. R.G.T. Geesink, K. De Groot, and P.A.K.T. Christel, Chemical Implant Fixation Using Hydroxyapatite Coatings, *Clin. Orthop. Relat. Res.*, 1987, **225**, p 147-170
36. B.C. Wang, E. Chang, C.Y. Yang, D. Tu, and C.H. Tasi, Characteristics and Osteoconductivity of Three Different Plasma-Sprayed Hydroxyapatite Coatings, *Surf. Coat. Technol.*, 1993, **58**(2), p 107-117
37. E. Munting, M. Verhelpen, F. Li, and A. Vincent, *CRC Handbook of Bioactive Ceramics*, T. Yamamuro, L.L. Hench, and J. Wilson, Ed., CRC Press, FL, 1990, p 143-148
38. K. de Groot, C.P.A.T. Klein, J.G.C. Wolke, and J.M.A. de Blieck-Hogervorst, *CRC Handbook of Bioactive Ceramics*, T. Yamamuro, L.L. Hench, and J. Wilson, Ed., CRC Press, FL, 1990, p 133-142
39. H. Ji and P.M. Marquis, Effect of Heat Treatment on the Microstructure of Plasma-Sprayed Hydroxyapatite Coating, *Biomaterials*, 1993, **14**(1), p 64-68
40. M.J. Filiaggi, N.A. Coombs, and R.M. Pilliar, Characterization of the Interface in the Plasma-Sprayed HA Coating/Ti-6Al-4V Implant System, *J. Biomed. Mater. Res.*, 1991, **25**(10), p 1211-1229
41. W.H. Duckworth, Discussion of Ryshkewitch Paper, *J. Am. Ceram. Soc.*, 1953, **36**(2), p 68
42. G. Jiang and D. Shi, Coating of Hydroxyapatite on Highly Porous Al_2O_3 Substrate for Bone Substitutes, *J. Biomed. Mater. Res. (Appl. Biomat.)*, 1998, **43**(1), p 77-81
43. Y.C. Yang, E. Chang, B.H. Hwang, and S.Y. Lee, Biaxial Residual Stress States of Plasma-Sprayed Hydroxyapatite Coatings on Titanium Alloy Substrate, *Biomaterials*, 2000, **21**(13), p 1327-1337

44. H.C. Gledhill, I.G. Turner, and C. Doyle, Direct Morphological Comparison of Vacuum Plasma Sprayed and Detonation Gun Sprayed Hydroxyapatite Coatings for Orthopaedic Applications, *Biomaterials*, 1999, **20**(4), p 315-322
45. D. Gauthier, J.M. Bouler, E. Aguado, P. Pilet, and G. Daculsi, Macroporous Biphasic Calcium Phosphate Ceramics: Influence of Macropore Diameter and Macroporosity Percentage on Bone Ingrowth, *Biomaterials*, 1998, **19**(1-3), p 133-139
46. L. Pawlowski, *The Science and Engineering of Thermal Spray Coatings*, Wiley, Chichester, 1995, p 414
47. R.B. Heimann, Thermal Spraying of Biomaterials, *Surf. Coat. Technol.*, 2006, **201**(5), p 2012-2019
48. C. Kumar, S.K. Nandi, A. Dey, P. Mukherjee, B. Kundu, S. Roy, and D. Basu, Evaluation of Plasma Spray Coated Hydroxyapatite and Bi-Phasic Calcium Phosphate Coated Pin Intra-Medullarly for Repair of Bone Defects in Rabbit Model, *First International Conference on ''NANOBIO'' Tissue Engineering and Stem Cell Research Using Nanomaterials*, organized by the Amrita Centre for Nano Sciences and Amrita Institute of Medical Sciences, p 60 in Book of Abstracts, Kochi, India, 17-19 Feb, 2009
49. S. Paolom, L. Matteo, and B. Luca, Residual Stresses in Plasma Sprayed Partially Stabilised Zirconia TBCs: Influence of the Deposition Temperature, *Thin Solid Films*, 1996, **278**(1-2), p 96-103
50. S. Takeuchi, M. Ito, and K. Takeda, Modelling of Residual Stress in Plasma-Sprayed Coatings: Effect of Substrate Temperature, *Surf. Coat. Technol*, 1990, **43-44**(Part 1), p 426-435
51. H. Li, L.Z. Sun, J.B. Li, and Z.G. Wang, X-Ray Stress Measurement and FEM Analysis of Residual Stress Distribution Near Interface in Bonded Ceramic/Metal Compounds, *Scr. Mater.*, 1996, **34**(9), p 1503-1508
52. J.D. Lee, H.Y. Ra, K.T. Hong, and S.K. Hur, Analysis of Deposition Phenomena and Residual Stress in Plasma Spray Coatings, *Surf. Coat. Technol.*, 1992, **56**(1), p 27-37
53. C. Ergun, R.H. Doremus, and W.A. Lanford, Interface Reaction/Diffusion in Hydroxylapatite-Coated SS316L and CoCrMo Alloys, *Acta Mater.*, 2004, **52**(16), p 4767-4772
54. U. Senturk, R.S. Lima, C.R.C. Lima, and C.C. Berndt, Deformation of Plasma Sprayed Thermal Barrier Coatings, *J. Eng. Gas Turb. Power*, 2000, **122**(3), p 387-392
55. B.D. Ratner, A.S. Hoffman, F.J. Schoen, and J.E. Lemons, *Biomaterials Science: An Introduction to Materials in Medicine*, 2nd ed., Elsevier Academic Press, USA, 2004, p 143
56. A.R.J. Franco, G. Pintaúde, A. Sinatora, C.E. Pinedo, and A.P. Tschiptschin, The Use of a Vickers Indenter in Depth Sensing Indentation for Measuring Elastic Modulus and Vickers Hardness, *Mater. Res.*, 2004, **7**(3), p 483-491
57. J. Wen, Y. Leng, J. Chen, and C. Zhang, Chemical gradient in plasma-sprayed HA coatings, *Biomaterials*, 2000, **21**(13), p 1339-1343
58. C. Zhang, Y. Leng, and J. Chen, Elastic and Plastic Behavior of Plasma-Sprayed Hydroxyapatite Coatings on a Ti–6Al–4V Substrate, *Biomaterials*, 2001, **22**(11), p 1357-1363
59. K.A. Khor, H. Li, and P. Cheang, Characterization of the Bone-Like Apatite Precipitated on High Velocity Oxy-Fuel HVOF Sprayed Calcium Phosphate Deposits, *Biomaterials*, 2003, **24**(5), p 769-775
60. G.J. Cheng, D. Pirzada, M. Cai, P. Mohanty, and A. Bandyopadhyay, Bioceramic Coating of Hydroxyapatite on Titanium Substrate with Nd-YAG Laser, *Mater. Sci. Eng. C*, 2005, **25**(4), p 541-547
61. T.G. Nieh, A.F. Jankowski, and J. Koike, Processing and Characterization of Hydroxyapatite Coatings on Titanium Produced by Magnetron Sputtering, *J. Mater. Res.*, 2001, **16**(11), p 3238-3245
62. T.G. Nieh, B.W. Choi, and A.F. Jankowski, Synthesis and Characterization of Porous Hydroxyapatite and Hydroxyapatite Coatings, A report submitted to *Minerals, Metals, and Materials Society Annual Meeting and Exhibition*, New Orleans, LA, Feb 11-15, 2001
63. R.W. Rice, Porosity Effects on Machining Direction-Strength Anisotropy and Failure Mechanisms, *J. Am. Ceram. Soc.*, 1994, **77**(8), p 2232-2236
64. H. Li, K.A. Khor, and P. Cheang, Young's Modulus and Fracture Toughness Determination of High Velocity Oxy-Fuel-Sprayed Bioceramic Coatings, *Surf. Coat. Technol.*, 2002, **155**(1), p 21-32
65. H. Li, K.A. Khor, and P. Cheang, Titanium Dioxide Reinforced Hydroxyapatite Coatings Deposited by High Velocity Oxy-Fuel HVOF Spray, *Biomaterials*, 2002, **23**(1), p 85-91
66. L. Fu, K.A. Khor, and J.P. Lim, Yttria Stabilized Zirconia Reinforced Hydroxyapatite Coatings, *Surf. Coat. Technol.*, 2000, **127**(1), p 66-75
67. L. Fu, K.A. Khor, and J.P. Lim, Processing, Microstructure and Mechanical Properties of Yttria Stabilized Zirconia Reinforced Hydroxyapatite Coatings, *Mater. Sci. Eng. A*, 2001, **316**(1-2), p 46-51
68. M. Wang, X.Y. Yang, K.A. Khor, and Y. Wang, Preparation and Characterization of Bioactive Monolayer and Functionally Graded Coatings, *J. Mater. Sci.: Mater. Med.*, 1999, **10**(5), p 269-273
69. K. Balani, R. Anderson, T. Laha, M. Andara, J. Tercero, E. Crumpler, and A. Agarwal, Plasma-Sprayed Carbon Nanotube Reinforced Hydroxyapatite Coatings and Their Interaction with Human Osteoblasts In Vitro, *Biomaterials*, 2007, **28**(4), p 618-624
70. K. Cheng, S. Zhang, W. Weng, K.A. Khor, S. Miao, and Y. Wang, The Adhesion Strength and Residual Stress of Colloidal-Sol Gel Derived β-Tricalcium-Phosphate/Fluoridated-Hydroxyapatite Biphasic Coatings, *Thin Solid Films*, 2008, **516**(10), p 3251-3255